

## THE MASS OF THE CENTRAL BLACK HOLE IN THE NEARBY SEYFERT GALAXY NGC 5273

MISTY C. BENTZ<sup>1</sup>, DANIEL HORENSTEIN<sup>1</sup>, CRAIG BAZHAW<sup>1</sup>, EMILY R. MANNE-NICHOLAS<sup>1</sup>, BENJAMIN J. OU-YANG<sup>1</sup>,  
MATTHEW ANDERSON<sup>1</sup>, JEREMY JONES<sup>1</sup>, RYAN P. NORRIS<sup>1</sup>, J. ROBERT PARKS<sup>1</sup>, DICY SAYLOR<sup>1</sup>, KATHERINE G. TEEMS<sup>1</sup>,  
CLAY TURNER<sup>1</sup>

(Received; Accepted)  
Draft version June 15, 2021

### ABSTRACT

We present the results of a reverberation-mapping program targeting NGC 5273, a nearby early-type galaxy with a broad-lined active galactic nucleus. Over the course of the monitoring program, NGC 5273 showed strong variability that allowed us to measure time delays in the responses of the broad optical recombination lines to changes in the continuum flux. A weighted average of these measurements results in a black hole mass determination of  $M_{\text{BH}} = (4.7 \pm 1.6) \times 10^6 M_{\odot}$ . An estimate of the size of the black hole sphere of influence in NGC 5273 puts it just at the limit of the resolution achievable with current ground-based large aperture telescopes. NGC 5273 is therefore an important future target for a black hole mass determination from stellar dynamical modeling, especially because it is the only nearby early-type galaxy hosting an AGN with a reverberation-based mass, allowing the best comparison for the masses determined from these two techniques.

*Subject headings:* galaxies: active — galaxies: nuclei — galaxies: Seyfert

### 1. INTRODUCTION

Over the last  $\sim 25$  years, observational and computational studies have led to the widely accepted belief that supermassive black holes (black holes with masses  $M_{\text{BH}} = 10^6 - 10^{10} M_{\odot}$ ) play a significant role in galaxy evolution and cosmology. To truly understand the physical processes at play in an active galactic nucleus (AGN) and the effects on the host galaxy and its surroundings, it is necessary to know the mass of the central black hole that is involved.

Currently, it is only feasible to directly measure black hole masses in relatively nearby galaxies through dynamical modeling (which is limited by spatial resolution) or reverberation mapping (which is limited by time). For quiescent galaxies,  $M_{\text{BH}}$  is derived from modeling the dynamics of stars and/or gas on parsec scales in a galaxy nucleus (e.g., Gültekin et al. 2009; McConnell & Ma 2013). For AGNs, the response of milliparsec-scale gas in the broad line region (BLR) to the accretion disk flux variability probes the gravitational force of the black hole in a technique known as reverberation mapping (e.g., Peterson et al. 2004). Dynamical studies rely on spatial resolution and are therefore limited to the most nearby galaxies ( $\lesssim 100 - 150$  Mpc). Reverberation mapping relies on temporal resolution and is not inherently distance limited, but timing arguments and resource availability have generally limited reverberation studies to  $z < 0.1$  ( $\sim 400$  Mpc). The  $M_{\text{BH}}$  measurements that result from directly probing the gravity of the supermassive black hole through these techniques provide the foundation for all black hole scaling relations used to investigate  $M_{\text{BH}}$  at cosmological distances. As such, the  $M_{\text{BH}}$  estimates provided by the scaling relations are directly affected by the quality of the observations and measurements used to calibrate the relationships.

Both the dynamical and reverberation masses currently suffer from several inherent uncertainties and potential systematic biases (for recent discussions, see Graham et al. 2011 for the dynamical studies and Peterson 2010 for the reverberation studies). One of the most pernicious uncertainties affecting

reverberation masses is the exact translation from reverberation measurements to calibrated black hole mass. The so-called “f factor” is an order unity scaling factor that depends on the detailed geometrical and dynamical properties of the broad-line region gas that is used to probe the gravitational influence of the black hole. Recent progress has shown promise in constraining the “f factor” for individual reverberation targets with high-quality datasets (Pancoast et al. 2014).

What is currently lacking, however, is a set of black holes with both dynamical and reverberation masses that can be directly compared to ensure that all black hole masses are on the same mass scale. Only three AGNs in the current reverberation sample are close enough and have massive enough black holes that they can be investigated through stellar dynamical modeling — NGC 3227 (Davies et al. 2006), NGC 4151 (Onken et al. 2004, 2014), and NGC 6814 (Bentz et al. 2009b for the reverberation mass; observations of the dynamics in the galaxy nucleus are in progress at this time). Comparison of black hole masses derived from independent techniques in the same galaxies is an important cross check, because these black hole masses are the foundation upon which all scaling relationships are built. Stellar dynamical modeling, in particular, is often described as the “gold standard” of supermassive black hole masses. However, all stellar dynamical masses result from axisymmetric modeling codes that are unable to account for the unique dynamics that arise in the presence of a bar. NGC 3227, NGC 4151, and NGC 6814 are all late-type spiral galaxies with bars. Recently, Onken et al. (2014) showed that even the weak bar in NGC 4151 can induce a strong bias in the resultant black hole mass from stellar dynamical modeling, causing the black hole mass to be overestimated. This bias would not be expected to affect the reverberation masses, where the tracer particles or “test masses” are located much deeper in the gravitational potential well of the black hole, at distances of only a few light days ( $\sim 0.01$  pc for nearby Seyferts), where they would be unaffected by the dynamics of a galaxy-scale bar.

Motivated by the small number of AGNs with reverberation masses that are also suitable targets for dynamical studies, we have begun a program to identify and monitor all AGNs that

<sup>1</sup> Department of Physics and Astronomy, Georgia State University, 25 Park Place, Suite 600, Atlanta, GA 30303, USA; bentz@astro.gsu.edu

may be suitable for both reverberation and dynamical studies. The rarity of broad-lined AGNs in the local Universe is the fundamental limitation in this endeavor, as this rarity generally translates to a large distance and therefore an inability to spatially resolve the galaxy nucleus on the scales necessary for dynamical modeling. Our goal is to build the largest sample possible, although the sample is not likely to be larger than  $\sim 10$  AGNs given the current technological constraints. In this manuscript, we present a reverberation-based mass for the central black hole in NGC 5273, the first reverberation target in an early-type unbarred galaxy at a distance suitable for ground-based dynamical studies. In §2, we describe the observations, and in §3, the light curve analysis. The black hole mass determination is described in §4. Finally, we discuss the results of our analysis and summarize our findings in §5 and §6.

## 2. OBSERVATIONS

NGC 5273 is a broad-lined Seyfert located at RA = 13h42m08.3s, Dec = +35°39'15", and  $z = 0.00362$ . The host galaxy morphology is S0 and it exhibits a faint spiral structure. The distance to NGC 5273 has been determined from surface brightness fluctuations of the host galaxy (Tonry et al. 2001, recalibrated by Tully et al. 2008) and is found to be  $16.5 \pm 1.6$  Mpc.

### 2.1. Spectroscopy

Spectroscopic monitoring of NGC 5273 was carried out at the Apache Point Observatory 3.5 m telescope from 2014 May 14 – July 1 (UT dates here and throughout). The monitoring program was scheduled for the first hour of almost every night during this time period, resulting in observations being taken during evening twilight. The Dual Imaging Spectrograph (DIS) was employed with the low-resolution (B400 and R300) gratings and the 5" slit rotated to a position angle of 0° (oriented N–S). With central wavelengths of 4398 Å and 7493 Å, the spectra span the entire optical bandpass from the atmospheric cutoff to 1 micron with a nominal dispersion of 1.8 Å/pix and 2.3 Å/pix, respectively. A single spectrum with a typical exposure time of 420 s was obtained each night the weather permitted, except for a span of 4 nights in June when the target was above the 85° altitude limit of the telescope during the time constraints of our program. The spectrophotometric standard star, Feige 66, was also observed throughout this campaign, as were two additional AGNs (we will describe their results elsewhere).

Spectra were reduced and flux calibrated following standard procedures. An extraction width of 12 pixels was used, corresponding to an angular width of 5" and 4.8" for the blue and red sides, respectively. The regions for background subtraction determination were set on either side of the spectrum between 75–95 pixels ( $\sim 30$ –40 arcsec) from the nucleus.

Spectroscopic monitoring campaigns generally do not enjoy the luxury of photometric conditions every night, so the rough flux calibration obtained with a spectrophotometric standard star is not accurate enough to measure the few-percent variations we expect during a reverberation campaign. A final, internal calibration of the spectra is required. We follow the typical procedure, which is to intercalibrate the spectra with the scaling method of van Groningen & Wanders (1992) by assuming a constant flux in the narrow emission lines. A reference spectrum is built from the user-determined best spectra, and the differences between each individual spectrum

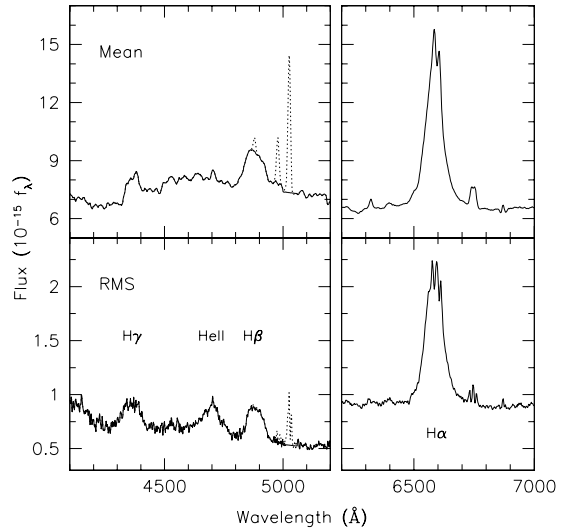


FIG. 1.— Mean and root-mean-square (RMS) spectra of NGC 5273 created from the 30 individual spectra collected throughout the monitoring campaign. The solid line shows the narrow-line subtracted spectra, and the dotted line shows the spectra with the narrow lines included. The RMS spectrum displays the variable components of the spectra. The broad-emission lines are clearly visible, including He II which is quite difficult to see in the mean spectrum. The host-galaxy features and narrow emission lines, which we expect to be constant on these timescales, are generally absent in the RMS spectrum except for some residual noise.

and the reference are minimized in the  $\lambda\lambda 4959, 5007$  region. This method accounts for small differences in wavelength calibration, spectral resolution, and flux calibration from night to night and has been shown to result in relative spectrophotometry that is accurate to 2% (Peterson et al. 1998a). While variability of AGN narrow emission lines has been detected (Peterson et al. 2013), the timescale of variation was much longer (a few years) than the timescales probed by typical reverberation-mapping campaigns such as the one we present here. For the red spectra, we instead used the [S II] doublet for the internal calibration. The weakness of these emission lines relative to H $\alpha$  resulted in a less accurate calibration for the spectra and noisier light curves, but we were still able to measure a mean time delay, as we discuss in §3.

Figure 1 shows the final mean and root-mean-square (RMS) of the 30 calibrated spectra collected over the 7 week period of our monitoring program. The Balmer lines H $\alpha$ , H $\beta$ , and H $\gamma$ , as well as He II  $\lambda 4686$  are clearly visible in the RMS spectrum, evidencing their large variability during the monitoring campaign. Based on the nights where our campaign enjoyed the best weather and observing conditions, we measured a mean integrated flux of  $f = 93.2 \pm 0.6 \times 10^{-15}$  ergs s $^{-1}$  cm $^{-2}$  for the [O III]  $\lambda 5007$  emission line, which agrees well with the value of  $89.9 \times 10^{-15}$  ergs s $^{-1}$  cm $^{-2}$  determined by the Sloan Digital Sky Survey (Ahn et al. 2014) and sets the absolute flux scale of our spectra.

### 2.2. Photometry

Photometric monitoring was carried out at two observatories through the months of 2014 May and June. We obtained test observations on 2014 April 26 and began nightly monitoring on 2014 May 4 at Georgia State University’s Hard Labor Creek<sup>2</sup> Observatory in Hard Labor Creek State Park near Rutledge, GA. Even with the unpredictable spring weather, we

<sup>2</sup> The origins of the name for Hard Labor Creek are unclear, but a Wikipedia entry links the etymology to either the slaves who labored in the

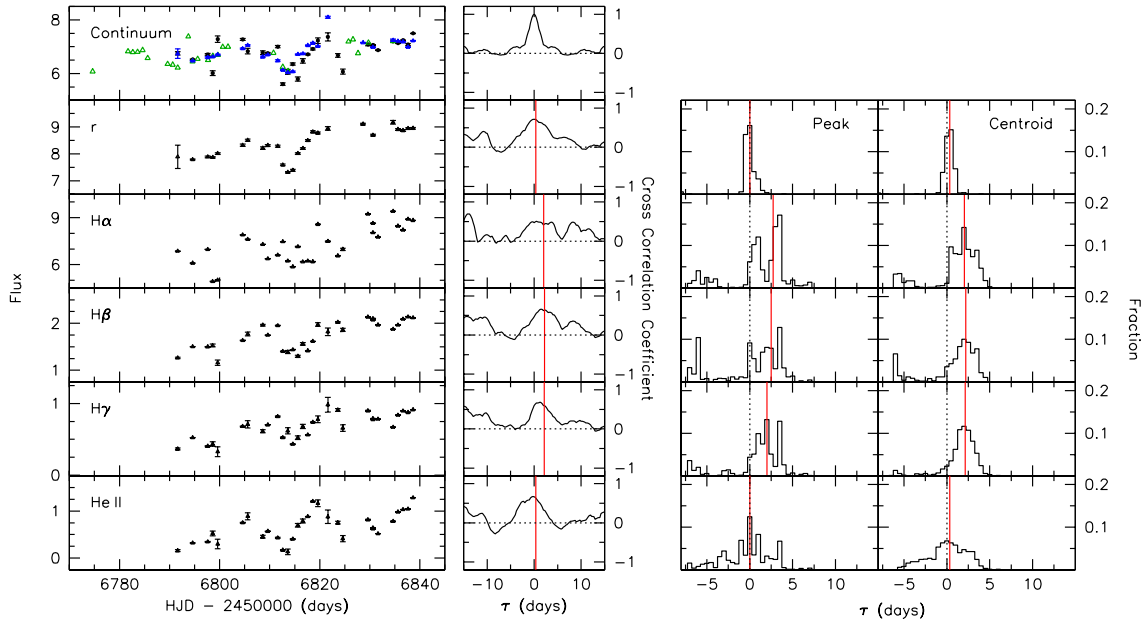


FIG. 2.— (*Left:*) Light curves and their corresponding cross-correlation functions relative to the continuum. For the continuum light curve, this is the auto-correlation function. The black points in the continuum box represent the  $\lambda 5100 \text{ \AA}$  flux density, while the green triangles represent the HLCO  $V$ -band photometry and the blue points represent the APO  $g$ -band photometry. The red vertical lines in the cross-correlation plots show the value of  $\tau_{\text{cent}}$  measured for each light curve from the distributions built up through the Monte Carlo techniques described in the text. (*Right:*) Cross-correlation peak distributions and cross-correlation centroid distributions from which the mean time delays and their uncertainties are determined.

were able to obtain photometry on nearly half (25/59) of the nights. Images were acquired with the 24-inch Miller Telescope and the Apogee  $2048 \times 2048$  detector through a Johnson  $V$ -band filter. The detector spans a field-of-view of  $26'.3 \times 26'.3$  with a pixel size of  $0''.77$ . Typical exposure times were 180 s, and three dithered images were generally taken at the position of NGC 5273. Images were reduced following standard procedures in IRAF.<sup>3</sup>

$V$ -band light curves were derived from the individual images by registering all images to a common alignment using *Sexterp* (Sivert et al. 2012) and applying the image subtraction software package *ISIS* (Alard & Lupton 1998; Alard 2000). *ISIS* builds a reference frame from the images (defined by the user) with the best seeing and lowest background levels. It then uses a spatially-variable kernel to convolve the reference frame to match the point spread function (PSF) of each individual image. Subtracting the convolved reference frame leaves behind residuals that show any regions of variability. The light curve was measured from the subtracted images, and therefore does not include any constant flux components such as the contribution from the host galaxy starlight.

Photometry was also obtained at the Apache Point Observatory 3.5 m telescope in New Mexico. A 30 s image was typically obtained immediately following readout of the spectra. The two arms of the DIS instrument allowed two images — Gunn-Thuan  $g$  and  $r$  bands — to be obtained simultaneously with the blue and red cameras. On a few nights, images were not obtained after the spectra. These nights were

nearby cotton fields, or to the Native Americans who had difficulties fording the creek.

<sup>3</sup> IRAF is distributed by the National Optical Astronomy Observatory, which is operated by the Association of Universities for Research in Astronomy (AURA) under cooperative agreement with the National Science Foundation.

typically partly cloudy, leading to a delay in pointing and focusing the telescope and shortening the on-sky time for our program. Images were reduced in IRAF following standard procedures. The narrow field of view ( $\sim 4'.1 \times 6'.9$ ) and small number of field stars in each DIS image precluded the use of image subtraction techniques. Instead, we carried out aperture photometry of NGC 5273 and a comparison field star  $132''$  to the southwest (SDSS J134202.91+353721.6). We employed circular apertures with radii of  $2''.1$  ( $g$ ) and  $2''.0$  ( $r$ ), and sky annuli of  $4''.6 - 5''.9$  ( $g$ ) and  $4''.4 - 5''.6$  ( $r$ ).

### 3. LIGHT CURVE ANALYSIS

Emission-line light curves were determined from the final, scaled spectra by fitting a local, linear continuum under each emission line and integrating the line flux above this continuum. We do not follow the procedure of fitting the entire spectrum with model components because the results are very sensitive to the exact parameters that are included and how they are modeled (Denney et al. 2009). The light curve for the continuum flux density at  $5100 \text{ \AA} \times (1+z)$  was also measured. Table 1 gives our tabulated spectroscopic and photometric light curves.

The  $V$ -band filter ( $\lambda_c = 5483 \text{ \AA}$  and  $\Delta\lambda = 827 \text{ \AA}$ ) does not include a significant contribution from any of the broad emission lines in the spectrum of NGC 5273, so we combined the  $V$ -band photometry with the  $5100 \text{ \AA}$  continuum flux densities. We identified pairs of points in the two light curves that were contemporaneous within 0.75 days. A linear relationship was then fit to the pairs of points to determine the multiplicative and additive factors necessary to bring the  $V$ -band fluxes into agreement with the  $5100 \text{ \AA}$  fluxes, taking into account the differences in galaxy background light and bandpass.

We then compared the merged continuum light curve with the Gunn-Thuan  $g$ - and  $r$ -band photometry from APO. We detected no significant time delay between the continuum and

the  $g$ -band, so we merged those light curves together in the same way. However, we did detect a small time delay between the continuum light curve and the  $r$ -band photometry (see Figure 2 and Table 3, so we did not merge the  $r$ -band with the continuum light curve. The small delay determined for the  $r$ -band is likely due to the strong contribution to the bandpass from the broad  $H\alpha$  emission line ( $\sim 90\%$  of the  $r$ -band flux, cf. Table 2). A similar effect would be expected from  $H\beta$  for the  $g$ -band, but the smaller equivalent width of  $H\beta$  relative to the total bandpass ( $\sim 40\%$  of the  $g$ -band flux) is likely the reason we did not detect any time delay for  $g$ .

Figure 2 shows the light curves for the continuum (including the  $V$ -band and  $g$ -band photometry), the  $r$ -band photometry, and for the optical recombination lines  $H\alpha$ ,  $H\beta$ ,  $H\gamma$ , and  $He II$ . NGC 5273 exhibited fairly strong variability over the course of the monitoring campaign. Table 2 gives the variability statistics for the final light curves displayed in Figure 2. Column (1) lists the spectral feature and column (2) gives the number of measurements in the light curve. Columns (3) and (4) list the average and median time separation between measurements, respectively. Column (5) gives the mean flux and standard deviation of the light curve, and column (6) lists the mean fractional error (based on the comparison of observations that are closely spaced in time). Column (7) lists the excess variance, computed as:

$$F_{\text{var}} = \frac{\sqrt{\sigma^2 - \delta^2}}{\langle F \rangle} \quad (1)$$

where  $\sigma^2$  is the variance of the fluxes,  $\delta^2$  is their mean-square uncertainty, and  $\langle F \rangle$  is the mean flux. And column (8) is the ratio of the maximum to the minimum flux in the light curve. In general, the true level of variability was somewhat higher than these measurements describe if taken at face value. The continuum light curve includes the host-galaxy starlight contribution, as does the  $r$ -band light curve. The broad emission-line light curves include the contribution from the narrow emission lines. These non-variable components serve to dampen the variations we observe in the light curves.

To determine the average time lag of the emission lines relative to the continuum, we first cross-correlated the light curves using the interpolation cross-correlation method (Gaskell & Sparke 1986; Gaskell & Peterson 1987) with the modifications of White & Peterson (1994). The method determines the cross-correlation function (CCF) twice: first, by interpolating the continuum light curve, and then by interpolating the emission-line light curve. The final CCF is the average of the two. We characterize the results of the CCF by recording the maximum value of the CCF ( $r_{\text{max}}$ ), the time delay of the CCF maximum ( $\tau_{\text{peak}}$ ) and the centroid of the points about the peak ( $\tau_{\text{cent}}$ ) above a threshold value of  $0.8r_{\text{max}}$ . CCFs for each light curve relative to the continuum are displayed in Figure 2.

To quantify the uncertainties on the time lag measurements, we employ the Monte Carlo “flux randomization/random subset sampling” method of Peterson et al. (1998b, 2004). From the  $N$  available data points, a selection of  $N$  points is chosen without regard to whether a datum has been previously selected. The uncertainty on a point that is sampled  $1 \leq n \leq N$  times is scaled by a factor of  $n^{1/2}$  and the typical number of points that is not sampled in any specific realization is  $\sim 1/e$ . This is the “random subset sampling”, and it quantifies the uncertainty that arises from the inclusion of any specific data point in the light curve. The flux values in the selected subset are then modified by a Gaussian deviation of the flux uncertainty. This is the “flux randomization” and it accounts

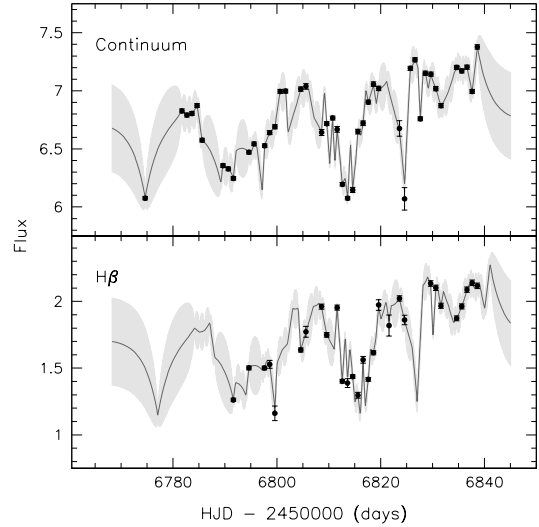


FIG. 3.— Continuum and  $H\beta$  light curves (data points) with the mean JAVELIN model (solid lines) and uncertainties (gray shaded regions). The uncertainties on the mean model are derived from the standard deviation of the individual realizations.

for the measurement uncertainties. The final sampled and modified light curves are then cross-correlated and the CCF measurements are recorded. The process is repeated many times ( $N = 1000$ ) and a distribution of CCF measurements are built up (see the right-hand panels in Figure 2). We take the means of the cross-correlation centroid distribution and the cross-correlation peak distribution as  $\tau_{\text{cent}}$  and  $\tau_{\text{peak}}$ , respectively. The uncertainties on  $\tau_{\text{cent}}$  and  $\tau_{\text{peak}}$  are determined so that 15.87% of the realizations fall above and 15.87% fall below the range of uncertainties, corresponding to  $\pm 1\sigma$  for a Gaussian distribution.

Table 3 lists the measured time lags and their uncertainties for the emission lines and for the  $r$ -band relative to the continuum light curve. We also investigated the time lags with the software package JAVELIN, previously known as SPEAR (Zu et al. 2011). JAVELIN uses a damped-random walk to fit the continuum light curve, and then determines the best model for the reprocessed (shifted and smoothed) emission-line light curves by maximizing the likelihood of the model. Uncertainties in the time delay are determined through a Bayesian Markov Chain Monte Carlo method.

Unfortunately, we were unable to obtain reasonable constraints on the smoothing and delay parameters when simultaneously modeling multiple emission-line light curves with JAVELIN. Instead, we ran multiple models and each time we focused on modeling the continuum and a single emission line. Figure 3 shows the modeling results obtained for the  $H\beta$  emission-line light curve. The time lags we obtained with JAVELIN were generally consistent with those determined through cross-correlation methods (see Table 3), but the difficulties we encountered leads us to focus on the time lags obtained through cross-correlation methods throughout the remainder of this manuscript.

Finally, we can compare the time delay measured for  $H\beta$  with that expected from the relationship between emission line time delay and AGN luminosity (the  $R_{\text{BLR}} - L$  relationship) determined for the full reverberation sample of AGNs. The  $5100 \text{ \AA}$  luminosity of NGC 5273 as determined from the mean spectrum contains a large contribution from host-galaxy starlight. Fortunately, the *Hubble Space Telescope* archive

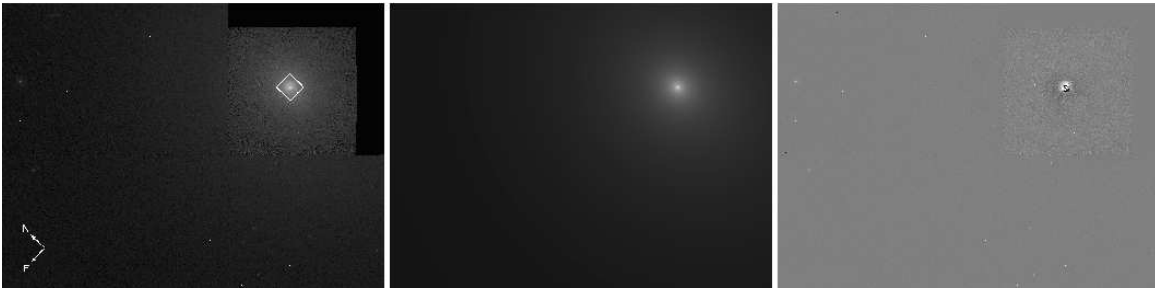


FIG. 4.— *HST* WFPC2 image of NGC 5273 with the  $5'' \times 5''$  spectroscopic monitoring slit geometry superposed (*left*). The best-fit model from two-dimensional surface brightness modeling with Galfit (*middle*) and the residuals after subtraction of the model from the image (*right*) are also shown. Regions with no data (such as the area outside the PC detector) were masked during the fitting process.

contains WFPC2 imaging of NGC 5273 through the F547M filter, which allowed us to determine the starlight correction and deduce the AGN luminosity. Following the methods of Bentz et al. (2013), we modeled the surface brightness distribution of the drizzled and combined WFPC2 image in two dimensions with Galfit (Peng et al. 2002, 2010). The galaxy was well fit with an exponential disk and a Sérsic bulge with index  $n = 3.3$ . The modeling allowed us to accurately subtract the AGN contribution and create a “PSF-free” image of NGC 5273, from which we determined the starlight flux through the monitoring aperture of  $(4.80 \pm 0.48) \times 10^{-15} \text{ ergs s}^{-1} \text{ cm}^{-1} \text{ \AA}$  at  $5100 \times (1+z) \text{ \AA}$ . The mean flux at  $5100 \text{ \AA}$  (as shown in Table 2) was corrected for the starlight contribution, giving an AGN luminosity of  $\log L_{\text{AGN}}/\text{ergs s}^{-1} = 41.534 \pm 0.144$ . Figure 5 shows our  $\text{H}\beta$  time delay measurement and starlight corrected luminosity for NGC 5273, which agrees well with the expectations from the  $R_{\text{BLR}} - L$  relationship.

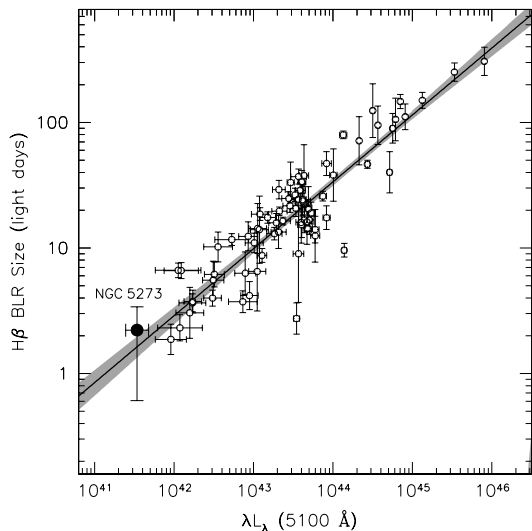


FIG. 5.— The  $\text{H}\beta$   $R_{\text{BLR}} - L$  relationship for the reverberation sample of AGNs. Open circles show the measured time delays and luminosities as tabulated in Bentz et al. (2013), and the power law and gray shaded region are the best fit and  $1\sigma$  uncertainty for the Bentz et al. (2013) compilation. The solid point shows our measurement of the  $\text{H}\beta$  time delay and starlight corrected luminosity for NGC 5273 from this work.

#### 4. LINE WIDTH MEASUREMENTS

The width of a broad emission line is a measure of the line-of-sight velocity of the gas in the broad line region. Narrow emission lines are emitted from gas that does not participate in the same bulk motion as the broad line region gas, so we

report the width of only the broad components of the emission lines.

Figure 1 shows the mean and RMS spectra for NGC 5273 (dotted lines) as well as the narrow-line subtracted mean and RMS spectra (solid lines). For the narrow line subtraction, we used the  $[\text{O III}] \lambda 5007$  emission line as a template for the  $\lambda 4959$  and  $\text{H}\beta$  narrow lines. The ratio of  $[\text{O III}] \lambda 4959/[\text{O III}] \lambda 5007$  was set at 0.34 (Storey & Zeippen 2000), and we derived a ratio of  $\text{H}\beta/[\text{O III}] \lambda 5007 = 0.10$ . Due to the lack of a suitable narrow emission line in the red spectra for use as a template, we did not attempt any narrow line subtraction with  $\text{H}\alpha$ .

The widths of the broad emission lines were measured in the narrow-line subtracted mean and RMS spectra and are reported as two separate measures: the full width at half-maximum (FWHM) flux, and the line dispersion,  $\sigma_{\text{line}}$ , which is the second moment of the emission-line profile (Peterson et al. 2004). The uncertainties in the line widths were set using a Monte Carlo random subset sampling method. In this case, from a set of  $N$  spectra, a random subset of  $N$  spectra were selected without regard to whether a spectrum had previously been chosen, and mean and rms spectra were created from the chosen subset. The FWHM and the  $\sigma_{\text{line}}$  were measured and recorded for each realization, and distributions of line-width measurements were built up over 1000 realizations. The mean and standard deviation of each distribution are taken to be the line width and uncertainty, respectively. This method quantifies the weight that any individual spectrum has on the final line width measurements. Additionally we also quantify the uncertainty from the exact placement of the continuum region on either side. For each line, we define a maximum continuum window (typically 30–50  $\text{\AA}$  wide) on either side of an emission line. For each realization, a subset of each continuum window of at least 7 pixels ( $\sim 14 \text{ \AA}$ ) is randomly selected, from which the local linear continuum is fit. This additional step has little effect on the RMS linewidths, because their uncertainties are dominated by the noise in the spectra, but has a small effect that increases the uncertainties we measure for the linewidths derived from the mean spectra (Bentz et al. 2009b).

Emission-line widths were corrected for the dispersion of the spectrograph following Peterson et al. (2004). Specifically, the observed line width  $\Delta\lambda_{\text{obs}}$  can be described as a combination of the intrinsic line width,  $\Delta\lambda_{\text{true}}$ , and the spectrograph dispersion,  $\Delta\lambda_{\text{disp}}$ , such that

$$\Delta\lambda_{\text{obs}}^2 \approx \Delta\lambda_{\text{true}}^2 + \Delta\lambda_{\text{disp}}^2. \quad (2)$$

We determined  $\Delta\lambda_{\text{true}}$  by taking our measurement of the FWHM of  $[\text{O III}] \lambda 5007$  as  $\Delta\lambda_{\text{obs}} = 14.26 \text{ \AA}$  and the FWHM measured by Whittle (1992) through a small slit and with

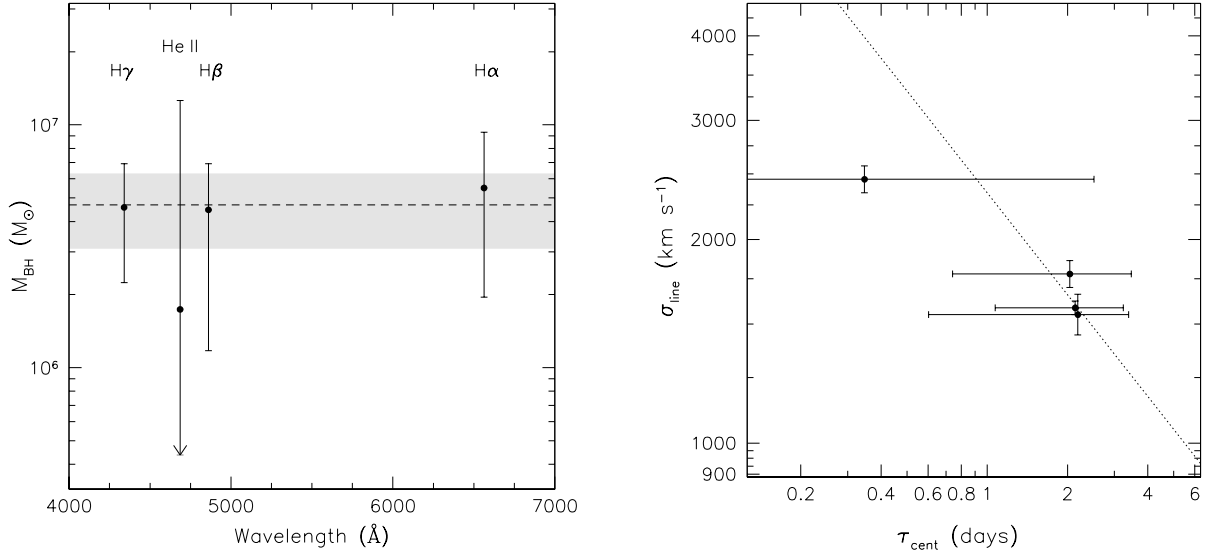


FIG. 6.— *Left*: Black hole masses derived from the emission line time delays and velocity widths. Each individual mass constraint is plotted at the central wavelength of the emission line from which it was derived. The dashed horizontal line and the shaded grey region show the weighted mean of the black hole mass and the  $1\sigma$  uncertainty, respectively. *Right*: Velocity widths of the emission lines compared to their measured time delays. The dotted line is not a fit to the points, but is a power law with slope of  $-0.5$  and intercept assuming the weighted mean black hole mass we have determined for NGC 5273. It shows the expected behavior for gas with motions dominated by the gravity of the black hole.

a high resolution as  $\Delta\lambda_{\text{true}} = 130 \text{ km s}^{-1}$ . We deduced a final spectral resolution of  $\Delta\lambda_{\text{disp}} = 14.1 \text{ \AA}$ , which we used to correct our line width measurements. The final rest-frame, resolution-corrected line width measurements determined from the mean and the RMS spectra are listed in Table 3.

### 5. BLACK HOLE MASS

The black hole mass is generally determined from reverberation-mapping measurements as:

$$M_{\text{BH}} = f \frac{c\tau V^2}{G} \quad (3)$$

where  $\tau$  is the time delay for a specific emission line relative to continuum variations, and  $V$  is the line-of-sight velocity width of the emission line, with  $c$  and  $G$  being the speed of light and gravitational constants, respectively. The emission-line time delay is therefore a measure of the responsivity-weighted average radius of the broad-line region for the emission of a particular species (e.g.,  $\text{H}\beta$ ). Only gas that is optically thick to ionizing radiation will be included in this measure, because optically thin gas will not respond to changes in the ionizing flux and will not reverberate.

The factor  $f$  includes the details of the inclination of the system to our line of sight and the exact geometrical arrangement of the responding gas, as well as its kinematics. These details are generally unknown for any particular object because the gas only extends across angular scales of milliarcseconds or less from our vantage point. Current practice is to apply a population-averaged value,  $\langle f \rangle$ , to reverberation masses to get the overall mass scale correct for the sample as a whole. The value of  $\langle f \rangle$  is determined from a comparison of the  $M_{\text{BH}} - \sigma_{\star}$  relationship for dynamical black hole masses and the  $M_{\text{BH}} - \sigma_{\star}$  relationship for AGNs with reverberation measurements. The overall multiplicative factor that must be applied to the AGN masses to bring the two relationships into agreement is taken to be  $\langle f \rangle$ . This value has varied in the literature from 5.5 (Onken et al. 2004) to 2.8 (Graham et al. 2011), depending on which objects are included

and the specifics of the measurements. We adopt the value determined by Grier et al. (2013) of  $\langle f \rangle = 4.3 \pm 1.1$  as it uses the most up-to-date set of measurements, and includes four high-luminosity AGNs with large  $M_{\text{BH}}$  that better anchor the high-mass end of the AGN  $M_{\text{BH}} - \sigma_{\star}$  relationship.

While the use of the  $M_{\text{BH}} - \sigma_{\star}$  relationship to set the absolute mass scale for reverberation masses has been fairly standard for the past 10 years, we note that there are several potential problems with this method. In particular, several studies have uncovered large scatter and morphological biases in the  $M_{\text{BH}} - \sigma_{\star}$  relationship for quiescent galaxies (e.g., Hu 2008; Graham et al. 2011; Kormendy et al. 2011). There are several lines of evidence that demonstrate, however, that adopting a mean scaling factor from comparison of  $M_{\text{BH}} - \sigma_{\star}$  relationships does put reverberation masses in the correct vicinity. Bentz et al. (2009a) compared the  $M_{\text{BH}} - L_{\text{bulge}}$  relationship for reverberation-mapped AGNs and quiescent galaxies and found that the two relationships were consistent when an average scaling factor determined from the  $M_{\text{BH}} - \sigma_{\star}$  relationship was adopted. Pancoast et al. (2014) directly determined AGN black hole masses through dynamical modeling of reverberation-mapping spectra and found an average  $\langle f \rangle = 4.8$  for the five AGNs they examined. They were also able to constrain the AGN inclinations, one of the largest expected contributions to the value of  $\langle f \rangle$ , and found inclinations of  $10 - 50^\circ$  to our line of sight. This agrees well with the inclination of  $\sim 29^\circ$  implied by a scaling factor of  $\langle f \rangle = 4.3$ , if other effects are neglected. Additionally, Fischer et al. (2013) analyzed the spatially-resolved biconical narrow line regions of several nearby AGNs with three-dimensional geometric models and found that the Seyfert 1s in their sample had inclinations to our line of sight of  $12 - 49^\circ$  with an average inclination of  $\sim 24^\circ$ . All of these independent studies suggest that adopting  $\langle f \rangle = 4.3$  for reverberation masses will result in a sample of unbiased masses, although the mass of any particular AGN is likely only accurate to a factor of 2-3.

Each emission line in our analysis provides an independent measurement of the black hole mass in NGC 5273. We can investigate the reliability of a reverberation-based black hole

mass determination by comparing the results for all the emission lines. Figure 6 (left) shows the black hole mass derived from the time delay and line width of each of the optical recombination lines we were able to probe: H $\alpha$ , H $\beta$ , H $\gamma$ , and He II. The right panel of Figure 6 shows the emission line width versus the time delay for each line. The dotted line is a power law with slope of  $-0.5$  which is the expected relationship if the gravity of the black hole dominates the dynamics of the gas we are probing. The results are consistent with the expectation, as has been seen for other reverberation studies (e.g., Peterson et al. 2004; Bentz et al. 2009b).

Combining our time lags ( $\tau_{\text{cent}}$ ) and line widths ( $\sigma_{\text{line,rms}}$ ) for each emission line and scaling by  $\langle f \rangle$ , we determine a final weighted mean of the black hole mass in NGC 5273 of  $M_{\text{BH}} = (4.7 \pm 1.6) \times 10^6 M_{\odot}$ .

## 6. DISCUSSION

The sphere of influence of the black hole is generally defined as:

$$r_h = \frac{GM_{\text{BH}}}{\sigma_*^2} \quad (4)$$

and it is a useful metric for comparing with the spatial resolution of stellar dynamical observations, to determine whether or not a reliable black hole mass is likely to be obtained from dynamical modeling.

NGC 5273 was included in the ATLAS<sup>3D</sup> (Cappellari et al. 2011) sample of early-type galaxies. Cappellari et al. (2013) derive a bulge stellar velocity dispersion of  $\sigma(R_e/8) = 74.1 \pm 3.7 \text{ km s}^{-1}$  from integral-field spectroscopy of the galaxy. Combined with the black hole mass we have derived here, we estimate  $r_h = 0.05''$ . This estimate depends rather sensitively on the specific value of  $\langle f \rangle$  that is adopted. Figure 7 shows where NGC 5273 lies on the most recent  $M_{\text{BH}} - \sigma_*$  relationship for AGNs, as determined by Grier et al. (2013). NGC 5273 sits slightly above the relationship, however it is within the scatter, lending credence to the value of  $M_{\text{BH}}$  determined here with  $\langle f \rangle = 4.3$ .

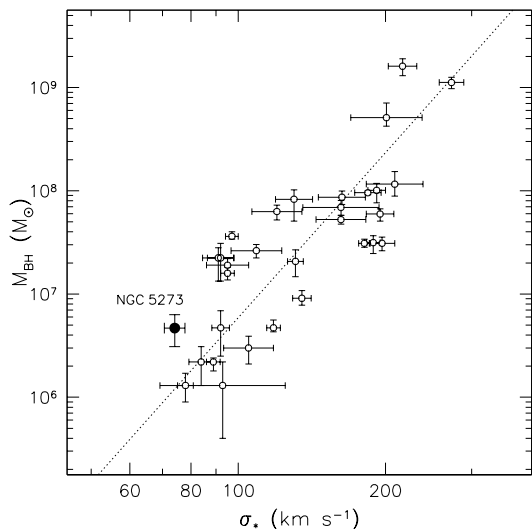


FIG. 7.— The  $M_{\text{BH}} - \sigma_*$  relationship for AGNs from Grier et al. (2013) with the best-fit relationship found for quiescent galaxies with dynamical masses (Woo et al. 2013). The solid point is our measurement for NGC 5273. While slightly above the relationship, NGC 5273 is within the scatter exhibited by the other AGNs.

of obtaining spatial resolutions of  $\sim 0.08''$  in the near-infrared with adaptive optics and integral-field units. The James Webb Space Telescope (JWST) will be able to achieve a similar resolution, but will have the added advantage of being located above the Earth’s atmosphere, allowing for a much lower background and a more stable PSF with a significantly higher Strehl ratio. Gültekin et al. (2009) show that a strict insistence on resolving  $r_h$  is not necessary for determination of an accurate stellar dynamical mass, which seems to be evidenced by the quality of the dynamical mass obtained for NGC 3227 (where  $r_h$  is not resolved; Davies et al. 2006). The early-type host galaxy of NGC 5273 makes it the ideal candidate for stellar dynamical modeling in order to directly test the masses obtained from reverberation mapping and those obtained from stellar dynamical modeling.

It is interesting that NGC 5273 sits above the relationship, as it is hosted by an early-type galaxy. The AGNs sitting slightly below the relationship at similar black hole masses all live in barred spiral galaxies, and Hu (2008) and Graham et al. (2011) have found that barred or pseudobulge galaxies have black hole masses that lie preferentially below the  $M_{\text{BH}} - \sigma_*$  relationship for early-type galaxies. It is currently unclear, however, whether this is because the black holes are undermassive or because the bar dynamics are artificially broadening the bulge stellar absorption line signatures in the spectra. The majority of the bulge stellar velocity dispersions in the AGN sample with reverberation masses are determined from fitting the stellar absorption lines in a single long slit spectrum, so it is likely that there is contamination from the bar dynamics in many of the stellar velocity dispersion measurements for the AGNs. Grier et al. (2013) attempted to quantify such a bias, but were unable to detect it among the current sample. On the other hand, Onken et al. (2014) found that using an axisymmetric dynamical modeling code to determine a stellar dynamical black hole mass could lead to a biased black hole mass measurement in barred galaxies, although in the case of NGC 4151, the object in their study, the bias led to an *overestimate* of  $M_{\text{BH}}$ , not an underestimate. Clearly, additional study is necessary to determine the exact effects caused by galaxy bars on black hole mass determinations, and NGC 5273 is an important addition to the reverberation sample given its proximity and the unbarred early-type morphology of its host galaxy.

## 7. SUMMARY

We have carried out a spectroscopic and photometric monitoring campaign of the AGN in the nearby Seyfert galaxy NGC 5273. From the time delays measured between the broad optical recombination lines and the continuum flux, we determine a black hole mass of  $M_{\text{BH}} = (4.7 \pm 1.6) \times 10^6 M_{\odot}$ . Combined with the bulge stellar velocity dispersion, we estimate that the black hole sphere of influence for NGC 5273 should be just at the limit of the resolution achievable with current ground-based instrumentation and with the integral field capabilities of JWST. NGC 5273 is the newest addition to a very short list of AGNs with reverberation-based masses and black hole spheres of influence capable of being probed with current technology. It is also the only one of these few AGNs in an early-type unbarred galaxy, which makes NGC 5273 an obvious candidate for stellar dynamical modeling for a direct comparison of the black hole masses determined from different techniques.

Current ground-based large-aperture telescopes are capable

We thank the anonymous referee for comments and sug-

gestions that improved the presentation of this manuscript. We thank Chris Onken, Kelly Denney, Kate Grier, Gisella de Rosa, and Ying Zu for helpful feedback and discussions. This research is based on observations obtained with the Apache Point Observatory 3.5-meter telescope, which is owned and operated by the Astrophysical Research Consortium. We heartily thank the staff at APO — especially telescope operators Alaina, Alysha, Jack, and Russet — for all their help

with this program. It was a pleasure to interact with y'all every night for two months! MCB gratefully acknowledges support from the NSF through CAREER grant AST-1253702. This research has made use of the NASA/IPAC Extragalactic Database (NED) which is operated by the Jet Propulsion Laboratory, California Institute of Technology, under contract with the National Aeronautics and Space Administration and the SIMBAD database, operated at CDS, Strasbourg, France.

## REFERENCES

- Ahn, C. P., Alexandroff, R., Allende Prieto, C., et al. 2014, *ApJS*, 211, 17  
 Alard, C. 2000, *A&AS*, 144, 363  
 Alard, C., & Lupton, R. H. 1998, *ApJ*, 503, 325  
 Bentz, M. C., Denney, K. D., Grier, C. J., et al. 2013, *ApJ*, 767, 149  
 Bentz, M. C., Peterson, B. M., Pogge, R. W., & Vestergaard, M. 2009a, *ApJ*, 694, L166  
 Bentz, M. C., Walsh, J. L., Barth, A. J., et al. 2009b, *ApJ*, 705, 199  
 Cappellari, M., Emsellem, E., Krajnović, D., et al. 2011, *MNRAS*, 413, 813  
 Cappellari, M., McDermid, R. M., Alatalo, K., et al. 2013, *MNRAS*, 432, 1862  
 Davies, R. I., Thomas, J., Genzel, R., et al. 2006, *ApJ*, 646, 754  
 Denney, K. D., Peterson, B. M., Dietrich, M., Vestergaard, M., & Bentz, M. C. 2009, *ApJ*, 692, 246  
 Fischer, T. C., Crenshaw, D. M., Kraemer, S. B., & Schmitt, H. R. 2013, *ApJS*, 209, 1  
 Gaskell, C. M., & Peterson, B. M. 1987, *ApJS*, 65, 1  
 Gaskell, C. M., & Sparke, L. S. 1986, *ApJ*, 305, 175  
 Graham, A. W., Onken, C. A., Athanassoula, E., & Combes, F. 2011, *MNRAS*, 412, 2211  
 Grier, C. J., Martini, P., Watson, L. C., et al. 2013, *ApJ*, 773, 90  
 Gültekin, K., Richstone, D. O., Gebhardt, K., et al. 2009, *ApJ*, 698, 198  
 Hu, J. 2008, *MNRAS*, 386, 2242  
 Kormendy, J., Bender, R., & Cornell, M. E. 2011, *Nature*, 469, 374  
 McConnell, N. J., & Ma, C.-P. 2013, *ApJ*, 764, 184  
 Onken, C. A., Ferrarese, L., Merritt, D., et al. 2004, *ApJ*, 615, 645  
 Onken, C. A., Valluri, M., Brown, J. S., et al. 2014, *ApJ*, 791, 37  
 Pancoast, A., Brewer, B. J., Treu, T., et al. 2014, *MNRAS*, in press (astro-ph/1311.6475)  
 Peng, C. Y., Ho, L. C., Impey, C. D., & Rix, H. 2002, *AJ*, 124, 266  
 Peng, C. Y., Ho, L. C., Impey, C. D., & Rix, H.-W. 2010, *AJ*, 139, 2097  
 Peterson, B. M. 2010, in *IAU Symposium*, Vol. 267, IAU Symposium, ed. B. M. Peterson, R. S. Somerville, & T. Storchi-Bergmann, 151–160  
 Peterson, B. M., Denney, K. D., De Rosa, G., et al. 2013, *ApJ*, 779, 109  
 Peterson, B. M., Ferrarese, L., Gilbert, K. M., et al. 2004, *ApJ*, 613, 682  
 Peterson, B. M., Wanders, I., Bertram, R., et al. 1998a, *ApJ*, 501, 82  
 Peterson, B. M., Wanders, I., Horne, K., et al. 1998b, *PASP*, 110, 660  
 Siverd, R. J., Beatty, T. G., Pepper, J., et al. 2012, *ApJ*, 761, 123  
 Storey, P. J., & Zeppen, C. J. 2000, *MNRAS*, 312, 813  
 Tonry, J. L., Dressler, A., Blakeslee, J. P., et al. 2001, *ApJ*, 546, 681  
 Tully, R. B., Shaya, E. J., Karachentsev, I. D., et al. 2008, *ApJ*, 676, 184  
 van Groningen, E., & Wanders, I. 1992, *PASP*, 104, 700  
 White, R. J., & Peterson, B. M. 1994, *PASP*, 106, 879  
 Whittle, M. 1992, *ApJS*, 79, 49  
 Woo, J.-H., Schulze, A., Park, D., et al. 2013, *ApJ*, 772, 49  
 Zu, Y., Kochanek, C. S., & Peterson, B. M. 2011, *ApJ*, 735, 80



TABLE 1  
TABULATED LIGHT CURVES

HJD (days)	$\lambda 5100 \text{ \AA}^a$	H $\alpha^b$	H $\beta^b$	H $\gamma^b$	He II <sup>b</sup>	HJD (days)	$g$ (mag)	$r$ (mag)	HJD (days)	$V^c$
6791.6275	6.754 ± 0.064	6.857 ± 0.015	1.262 ± 0.013	0.367 ± 0.014	0.157 ± 0.022	6791.63	14.771 ± 0.047	14.169 ± 0.058	6774.6377	6.075 ± 0.010
6794.6247	6.523 ± 0.019	6.100 ± 0.001	1.502 ± 0.001	0.524 ± 0.001	0.319 ± 0.002	6794.63	14.846 ± 0.004	14.183 ± 0.003	6781.7165	6.827 ± 0.012
6797.6143	6.711 ± 0.036	6.974 ± 0.005	1.501 ± 0.005	0.404 ± 0.006	0.345 ± 0.009	6797.62	14.810 ± 0.007	14.169 ± 0.004	6782.6802	6.791 ± 0.010
6798.6200	6.013 ± 0.089	4.928 ± 0.022	1.529 ± 0.029	0.435 ± 0.032	0.526 ± 0.051	6798.62	14.803 ± 0.004	14.172 ± 0.004	6783.6364	6.805 ± 0.011
6799.6162	7.282 ± 0.118	5.019 ± 0.021	1.162 ± 0.055	0.329 ± 0.068	0.298 ± 0.102	6799.62	14.781 ± 0.006	14.152 ± 0.004	6784.6254	6.873 ± 0.011
6804.6151	7.270 ± 0.039	7.899 ± 0.003	1.636 ± 0.005	0.679 ± 0.006	0.751 ± 0.009	6804.62	14.720 ± 0.006	14.111 ± 0.005	6785.6180	6.575 ± 0.010
6805.6161	6.833 ± 0.105	7.619 ± 0.022	1.773 ± 0.041	0.710 ± 0.052	0.889 ± 0.075	6805.62	14.689 ± 0.006	14.087 ± 0.005	6789.6239	6.356 ± 0.010
6808.6199	6.780 ± 0.068	7.296 ± 0.007	1.961 ± 0.017	0.612 ± 0.021	0.456 ± 0.031	6808.62	14.804 ± 0.008	14.125 ± 0.006	6790.6528	6.328 ± 0.015
6809.6203	6.759 ± 0.025	6.371 ± 0.013	1.749 ± 0.002	0.702 ± 0.003	0.569 ± 0.004	6809.62	14.783 ± 0.005	14.112 ± 0.004	6791.6362	6.215 ± 0.015
6811.6170	7.001 ± 0.042	6.605 ± 0.003	1.953 ± 0.007	0.819 ± 0.009	0.429 ± 0.013	6811.62	14.845 ± 0.009	14.116 ± 0.005	6793.7453	7.381 ± 0.031
6812.6227	5.606 ± 0.044	7.466 ± 0.002	1.402 ± 0.007	0.524 ± 0.008	0.169 ± 0.012	6812.63	14.952 ± 0.005	14.211 ± 0.004	6794.6275	6.450 ± 0.012
6813.6205	6.066 ± 0.094	6.232 ± 0.020	1.388 ± 0.033	0.619 ± 0.042	0.133 ± 0.060	6813.62	14.982 ± 0.006	14.251 ± 0.004	6795.6200	6.543 ± 0.009
6814.6198	6.351 ± 0.041	5.865 ± 0.003	1.437 ± 0.006	0.433 ± 0.007	0.403 ± 0.010	6814.62	14.972 ± 0.008	14.240 ± 0.006	6797.7028	6.506 ± 0.009
6815.6210	5.796 ± 0.077	7.147 ± 0.030	1.297 ± 0.021	0.524 ± 0.026	0.698 ± 0.038	6815.62	14.778 ± 0.006	14.152 ± 0.004	6798.6235	6.653 ± 0.009
6816.6235	6.467 ± 0.082	6.180 ± 0.015	1.562 ± 0.025	0.680 ± 0.031	0.789 ± 0.044	6816.63	14.771 ± 0.006	14.127 ± 0.004	6799.6525	6.686 ± 0.009
6817.6217	6.712 ± 0.023	6.229 ± 0.007	1.416 ± 0.002	0.562 ± 0.002	0.884 ± 0.003	6817.63	14.690 ± 0.005	14.088 ± 0.004	6800.6366	6.995 ± 0.009
6818.6197	6.913 ± 0.035	6.187 ± 0.014	1.616 ± 0.004	0.738 ± 0.005	1.205 ± 0.008	6818.62	14.669 ± 0.006	14.048 ± 0.005	6801.6919	6.998 ± 0.010
6819.6240	7.225 ± 0.107	8.574 ± 0.025	1.974 ± 0.040	0.779 ± 0.047	1.168 ± 0.071	6819.63	14.698 ± 0.005	14.053 ± 0.004	6810.7598	6.766 ± 0.012
6821.6228	7.367 ± 0.150	7.487 ± 0.026	1.819 ± 0.079	0.982 ± 0.102	0.879 ± 0.144	6821.63	14.453 ± 0.008	14.033 ± 0.008	6812.6366	6.242 ± 0.009
6823.6191	6.676 ± 0.066	6.564 ± 0.018	2.022 ± 0.016	0.909 ± 0.021	0.753 ± 0.030	6828.64	14.664 ± 0.003	14.013 ± 0.004	6813.6908	6.087 ± 0.009
6824.6152	6.070 ± 0.097	6.978 ± 0.073	1.861 ± 0.036	0.657 ± 0.046	0.414 ± 0.067	6830.64	14.708 ± 0.004	14.063 ± 0.004	6825.7306	7.194 ± 0.011
6829.6377	7.080 ± 0.044	9.236 ± 0.010	2.134 ± 0.007	0.898 ± 0.007	0.815 ± 0.010	6834.64	14.642 ± 0.010	14.005 ± 0.008	6826.6271	7.268 ± 0.009
6830.6350	7.058 ± 0.017	8.046 ± 0.002	2.073 ± 0.001	0.777 ± 0.001	0.646 ± 0.001	6835.64	14.650 ± 0.004	14.037 ± 0.004	6827.6469	6.759 ± 0.002
6830.6425	7.051 ± 0.019	8.640 ± 0.002	2.102 ± 0.001	0.789 ± 0.001	0.620 ± 0.002	6836.64	14.656 ± 0.003	14.042 ± 0.004	6829.7274	7.148 ± 0.012
6831.6370	6.873 ± 0.018	7.770 ± 0.001	1.967 ± 0.001	0.783 ± 0.001	0.519 ± 0.002	6837.64	14.706 ± 0.004	14.033 ± 0.004	6834.6433	7.200 ± 0.010
6834.6380	7.200 ± 0.040	9.407 ± 0.008	1.873 ± 0.005	0.670 ± 0.005	0.781 ± 0.008	6838.64	14.647 ± 0.004	14.032 ± 0.004		
6835.6333	7.132 ± 0.016	8.467 ± 0.002	1.963 ± 0.001	0.838 ± 0.001	0.982 ± 0.001					
6836.6370	7.243 ± 0.015	8.216 ± 0.001	2.088 ± 0.001	0.896 ± 0.001	1.034 ± 0.001					
6837.6348	7.082 ± 0.040	8.904 ± 0.005	2.139 ± 0.006	0.874 ± 0.006	1.044 ± 0.009					
6838.6364	7.497 ± 0.013	8.825 ± 0.002	2.117 ± 0.001	0.913 ± 0.001	1.284 ± 0.001					

<sup>a</sup>The continuum emission is listed as the flux density at  $\lambda 5100 \text{ \AA} \times (1+z)$  in units of  $10^{-15} \text{ ergs s}^{-1} \text{ cm}^{-2} \text{ \AA}^{-1}$ .

<sup>b</sup>Emission-line light curves are listed as the integrated flux in units of  $10^{-13} \text{ ergs s}^{-1} \text{ cm}^{-2}$ .

<sup>c</sup> $V$ -band measurements listed here are scaled to match the continuum flux for contemporaneous observations.

TABLE 2  
LIGHT-CURVE STATISTICS

Time Series	$N$	$\langle T \rangle$ (days)	$T_{\text{median}}$ (days)	$\langle F \rangle^a$	$\langle \sigma_F / F \rangle$	$F_{\text{var}}$	$R_{\text{max}}$
Continuum	46	$1.4 \pm 1.1$	1.0	$6.80 \pm 0.40$	0.0025	0.059	$1.326 \pm 0.022$
$r$	26	$1.8 \pm 1.5$	1.0	$8.36 \pm 0.54$	0.0062	0.064	$1.254 \pm 0.011$
H $\alpha$	30	$1.6 \pm 1.2$	1.0	$7.27 \pm 1.19$	0.0019	0.164	$1.909 \pm 0.009$
H $\beta$	30	$1.6 \pm 1.2$	1.0	$1.74 \pm 0.29$	0.0097	0.171	$1.841 \pm 0.088$
H $\gamma$	30	$1.6 \pm 1.2$	1.0	$0.68 \pm 0.18$	0.0320	0.260	$2.988 \pm 0.695$
He II	30	$1.6 \pm 1.2$	1.0	$0.67 \pm 0.32$	0.0648	0.474	$9.640 \pm 4.309$

<sup>a</sup>Continuum flux density is in units of  $10^{-15}$  ergs  $\text{s}^{-1} \text{cm}^{-2} \text{\AA}^{-1}$  and emission line fluxes are in units of  $10^{-13}$  ergs  $\text{s}^{-1} \text{cm}^{-2}$ .

TABLE 3  
TIME LAGS, LINE WIDTHS, AND VIRIAL PRODUCTS

Line	Time Lags			Mean Line Width		RMS Line Width		$\frac{c \tau_{\text{cent}} \sigma_{\text{line, rms}}^2}{G}$ ( $10^6 M_{\odot}$ )
	$\tau_{\text{cent}}$ (days)	$\tau_{\text{peak}}$ (days)	$\tau_{\text{JAV}}$ (days)	$\sigma_{\text{line}}$ ( $\text{km s}^{-1}$ )	FWHM ( $\text{km s}^{-1}$ )	$\sigma_{\text{line}}$ ( $\text{km s}^{-1}$ )	FWHM ( $\text{km s}^{-1}$ )	
H $\alpha$	$2.06^{+1.42}_{-1.31}$	$2.75^{+1.00}_{-2.00}$	$2.44^{+0.15}_{-0.94}$	$1781 \pm 36$	$3032 \pm 54$	$1783 \pm 66$	$3579 \pm 145$	$1.28^{+0.89}_{-0.82}$
H $\beta$	$2.22^{+1.19}_{-1.61}$	$2.50^{+1.25}_{-2.00}$	$1.45^{+1.09}_{-0.15}$	$1821 \pm 53$	$5688 \pm 163$	$1544 \pm 98$	$4615 \pm 330$	$1.03^{+0.57}_{-0.76}$
H $\gamma$	$2.14^{+1.09}_{-1.08}$	$2.00^{+1.75}_{-1.00}$	$1.32^{+0.17}_{-0.67}$	$1378 \pm 55$	$4015 \pm 101$	$1600 \pm 54$	$4231 \pm 604$	$1.06^{+0.55}_{-0.54}$
He II	$0.35^{+2.17}_{-1.66}$	$0.00^{+3.00}_{-1.75}$	$-0.24^{+0.26}_{-0.28}$	...	...	$2201 \pm 102$	$4204 \pm 882$	$0.41^{+2.30}_{-1.92}$
$r$	$0.35^{+0.47}_{-0.59}$	$0.00^{+0.50}_{-0.25}$	$0.12^{+0.13}_{-0.13}$	...	...	...	...	...

NOTE. — Time lags are presented in the observed frame, but are corrected for cosmological dilation when calculating the virial product — a tiny effect that is much smaller than the uncertainties in the case of NGC 5273 with  $z = 0.00362$ .